Impact of fixation and paraffin embedding on mouse brain morphology: a synchrotron radiation-based tomography study

Rodgers, Griffin, Tanner, Christine, Schulz, Georg, Migga, Alexandra, Weitkamp, Timm, et al.

Griffin Rodgers, Christine Tanner, Georg Schulz, Alexandra Migga, Timm Weitkamp, Willy Kuo, Mario Scheel, Melissa Osterwalder, Vartan Kurtcuoglu, Bert Müller, "Impact of fixation and paraffin embedding on mouse brain morphology: a synchrotron radiation-based tomography study," Proc. SPIE 11840, Developments in X-Ray Tomography XIII, 118400P (9 September 2021); doi: 10.1117/12.2595144

SPIE.

Event: SPIE Optical Engineering + Applications, 2021, San Diego, California, United States

Impact of fixation and paraffin embedding on mouse brain morphology: a synchrotron radiation-based tomography study

Griffin Rodgers[a,b], Christine Tanner[a,b], Georg Schulz[a,b,c], Alexandra Migga[a,b], Timm Weitkamp[d], Willy Kuo[e,f], Mario Scheel[d], Melissa Osterwalder[a,b], Vartan Kurtcuoglu[e,f], and Bert Müller[a,b]

[a]Biomaterials Science Center, Department of Biomedical Engineering, University of Basel, 4123 Allschwil, Switzerland
[b]Biomaterials Science Center, Department of Clinical Research, University Hospital Basel, 4031 Basel, Switzerland
[c]Core Facility Micro- and Nanotomography, Department of Biomedical Engineering, University of Basel, 14, 4123 Allschwil, Switzerland
[d]Synchrotron Soleil, 91192 Gif-sur-Yvette, France
[e]The Interface Group, Institute of Physiology, University of Zurich, 8057 Zurich, Switzerland
[f]National Centre of Competence in Research, Kidney.CH, 8057 Zurich, Switzerland

ABSTRACT

Formalin fixation and paraffin embedding of post mortem tissue specimens is widely used for high-resolution neuroimaging with both conventional and X-ray virtual histology. The exchange of embedding solutions generates non-uniform brain shrinkage and changes relative tissue densities. We used synchrotron radiation-based X-ray micro computed tomography with 3 µm pixel size to visualize a single mouse brain at each step of the embedding process. The best tissue contrast was found after the ethanol dehydration or paraffin embedding steps. The shrinkage generated by these preparations was quantified with volumetric strain fields after non-rigid registration to the reference formalin-fixed brain. Follow-up imaging of two murine brains with 0.65 µm pixel size, one ethanol-dehydrated and one paraffin-embedded, paves the way for the creation of cellular-resolution full brain atlases with X-ray virtual histology.

Keywords: X-ray virtual histology, non-rigid registration, strain field, brain atlas, anatomy, contrast enhancement, neuroimaging

1. INTRODUCTION

Understanding the brain's structure-function relationship remains a challenge due to the brain's multiscale organization and diversity of cell types.[1] Current neuroimaging approaches include magnetic resonance imaging (MRI), light microscopy, and electron microscopy. MRI provides multi-modal *in vivo* or *in situ* volumetric imaging, however spatial resolution does not reach individual cells. Light microscopy provides cellular resolution in-plane, but the limited penetration depth of visible light necessitates serial sectioning for volumetric imaging. Optical sectioning is an alternative to physical sectioning,[2,3] but requires tissue clearing. Electron microscopy offers even higher spatial resolution, but even serial block-face electron microscopy for volumetric imaging[4] is limited for whole-brain mapping. Thus, three-dimensionally mapping the entire brain's cytoarchitecture presents a major challenge.

In recent years, developments in X-ray micro- and nanotomography have led to the rise of virtual histology.[5] In the context of neuroimaging, X-ray penetration depth circumvents physical sectioning[6] and short wavelengths provide spatial resolution below the limits of optical microscopy.[7,8] Nanotomography has been demonstrated

Further author information: (Send correspondence to G.R.) E-mail: griffin.rodgers@unibas.ch, Telephone: +41 61 207 54 38, www.bmc.unibas.ch

Developments in X-Ray Tomography XIII, edited by Bert Müller
Ge Wang, Proc. of SPIE Vol. 11840, 118400P · © 2021 SPIE
CCC code: 0277-786X/21/$21 · doi: 10.1117/12.2595144

for dense neuronal reconstruction[7,8] and there are efforts to extend imaging capabilities to macroscopic specimens.[9] Microtomography has already been shown to map brain cytoarchitecture within volumes of tens of cubic millimeters[10–14] and recent studies have shown feasibility of mapping the full mouse brain with sub-1 µm voxels.[15–18] Therefore, hard X-ray virtual histology is promising for cellular-resolution full-brain mapping, where an understanding of mesoscale cytoarchitecture can link microscopic and macroscopic organization of the brain.[19]

Conventional histology is the gold standard for evaluation of tissue health and morphology in research and diagnostics. The necessary tissue fixation and preparation steps alter the tissue from its native *in vivo* state, however. X-ray virtual histology is a non-destructive imaging modality that can be performed without staining, which is of high value to evaluate each intermediary tissue preparation step for conventional histology, including a characterization of the preparation-induced density[20] and morphology[21] changes throughout the brain. Here, we performed synchrotron radiation-based microtomography of an entire mouse brain at each step of the standard protocol for formalin fixation and paraffin embedding.[22–24] Non-rigid registration of the three-dimensional data with 3.1 µm-voxels allowed for evaluation of volumetric strain fields and a comparison of tissue contrast in corresponding anatomical regions. Follow-up measurements with 0.65 µm-voxels compared an ethanol-dehydrated mouse brain and a paraffin-embedded mouse brain to further probe contrast changes at the cellular level.

2. MATERIALS AND METHODS

2.1 Mouse brain preparation

For the initial experiment with 3.1 µm pixel size, the brain of a six-month-old female C57BL/6JRj mouse (Janvier Labs, Le Genest-Saint-Isle, France) was extracted and immersion-fixed with 4% formaldehyde / phosphate buffered saline after sacrifice. For the follow-up experiment with 0.65 µm pixel size, the brain of a one-year-old female C57BL/6JRj mouse (Janvier Labs, Le Genest-Saint-Isle, France) was extracted and transcardially perfused with 4% formaldehyde / phosphate buffered saline after sacrifice, then immersed in 4% formaldehyde / phosphate buffered saline. Both mouse brains collected for this study were excess from an experiment approved by the veterinary office of the Canton of Zurich (license number ZH067/17).

The paraffin embedding protocol was as follows:[25] the brain was immersed for two hours in 20 mL of 50%, 70%, 80%, 90%, and 100% ethanol, then xylene (Carl Roth GmbH, Karlsruhe, Germany). The brain was then transferred to liquid paraffin (ROTI® Plast, Carl Roth GmbH, Karlsruhe, Germany) for 2 hours before cooling to solidify the paraffin. The second brain followed the same protocol until 100% ethanol. The immersed samples were measured in a 1.5 mL Eppendorf tube that was filled with the appropriate solution.

2.2 Microtomography of the mouse brain with effective pixel size of 3.1 µm

Imaging of the same brain at each intermediate step of the paraffin embedding protocol was performed at the ANATOMIX beamline at Synchrotron SOLEIL (Gif-sur-Yvette, France).[26] An effective pixel size of 3.1 µm was achieved with a detector based on a 300 µm-thick LuAG scintillator coupled to a scientific CMOS camera (Hamamatsu Orca Flash 4.0 V2, 2048 × 2048 pixels, 6.5 µm physical pixel size) *via* a lens system made of two photo objectives in tandem geometry (Hasselblad HC 4/210 and HC 2.2/100, numerical aperture of 0.22) resulting in a magnification factor of 2.1.[27] Line pairs with period below 10 µm could be resolved in radiographs of a Siemens star. An effective mean photon energy of approximately 22 keV was achieved with an undulator gap of 10.3 mm and a 20 µm Au filter. A 675 mm propagation distance was selected to provide edge enhancement without blurring greater than two pixels.[28] An exposure time of 50 ms was selected, filling approximately half of the detector's dynamic range in flat-field images. Fly scans were made with 5900 projections around 360° with offset axis-of-rotation to double the field of view.[29,30]

A ring correction based on the procedures reported in refs. 31, 32 was applied prior to reconstruction. The projections were then Gaussian filtered with $\sigma = 1.25$ pixels. This filtering improves the contrast-to-noise ratio at the cost of spatial resolution.[33] The full resolution data along with 3×3 and 9×9 binned projections were reconstructed in `Matlab` (release R2020a, The MathWorks, Inc., Natick, USA) using a filtered back-projection algorithm with a Ram-Lak filter.

2.3 Registration and segmentation of the microtomography data

Non-rigid registration of the brain at each embedding step is described in refs. 22–24. Briefly, a registration pipeline was built using the open-source registration software `elastix`.[34,35] Our approach consisted of four steps: (1) manual similarity transform, (2) automatic affine registration, (3) automatic B-spline registration, (4) manual rigid post-alignment for visualization. The $3 \times 3 \times 3$ binned datasets were used for registration due to the large size of the unbinned datasets. The resulting transformations were then applied to the full resolution data. Registration accuracy is discussed in more detail in refs. 22–24.

Volumetric strain fields give the voxel-wise volume change from the transformation found during registration and are calculated using the determinant of the spatial Jacobian. We used the open-source software `transformix`[34,35] to generate volumetric strain fields.

Segmentations were used to visualize the data, quantify volume change, provide masks for the registration, and identify corresponding regions for analysis of density changes. These segmentations were based on semi-automatic region growing with manually defined seed points. The software `VGStudio MAX 2.1` (Volume Graphics, Heidelberg, Germany) was used for segmentation and volume rendering.

2.4 Follow-up microtomography of two mouse brains with effective pixel size of 0.65 µm

In order to perform a detailed comparison of the effect of ethanol dehydration and paraffin embedding on the microanatomy of the mouse brain, follow-up microtomography was performed with 0.65 µm-wide voxels. These measurements were also performed at the ANATOMIX beamline at Synchrotron SOLEIL (Gif-sur-Yvette, France).[26] The detector design was similar to that in Section 2.2, except a 20 µm LuAG scintillator was used with a 10× objective to achieve an effective pixel size of 0.65 µm.[27] The undulator gap was set to 5.5 mm and the beam was filtered with 20 µm Au and 100 µm Cu, resulting in an approximate mean photon energy of 27 keV. A propagation distance of 50 mm was selected based on the two-pixel blurring rule.[28] An exposure time of 100 ms was selected, filling approximately half of the detector's dynamic range in flat-field images. Mosaic-style acquisition[15] was used to capture the entire width of the mouse brain. Four 360° scans with offset axis-of-rotation were used to extend the field-of-view by a factor of eight. Fly scans were used with 9000 projections.

The projections were phase retrieved with Paganin's filter[36] due to the small pixel size and relatively high photon energy used. As the model assumptions were not strictly held and the δ/β ratio was not known *a priori*, a series of reconstructions were made with $\delta/\beta \in (48, 100, 200, 500)$. Prior to filtering, ring artefacts were removed by subtracting from each projection the mean of all projections (plus a scalar offset to avoid shifting the mean intensities). Tomographic reconstruction was performed using `tomopy` (version 1.4.2)[37] with the *gridrec* algorithm,[38] which gave approximately a 100-fold increase in reconstruction speed compared to the filtered back-projection for these large datasets.

3. RESULTS AND DISCUSSION

3.1 Volumetric strain fields for the ethanol-dehydrated and paraffin embedded mouse brain

After non-rigid registration, volumetric strain fields were calculated for the brain in ethanol and paraffin. The results are visualized in Figure 1 based on histograms and virtual coronal slices through the volumetric strain fields. The virtual slices are given with the same color map, which is displayed on the histograms. Note that volumetric strain of 0% represents no volume change from the formalin-fixed state. The mean volume change in ethanol (paraffin) was around −40% (−60%). Both show a distribution of volume change, with outer regions of the brain, e.g. the cerebral cortex, experiencing volumetric strain of about about −55% (−75%), while inner regions, e.g. the thalamus, experiencing about −25% (−45%) for ethanol dehydration (paraffin embedding). The pattern of brain shrinkage was similar for ethanol and paraffin. Anatomical regions could be distinguished based on volume change alone: (top row) the anterior commissure, corpus callosum, and caudoputamen had relatively small volume change compared to the isocortex; (middle row) the thalamus showed the smallest volume change, the hippocampus and caudoputamen had volume change close to the mean, and the isocortex had the most volume change; (bottom row) white matter and medulla had less volume change than the cerebellum, whose granular layer had less volume change than its molecular layer.

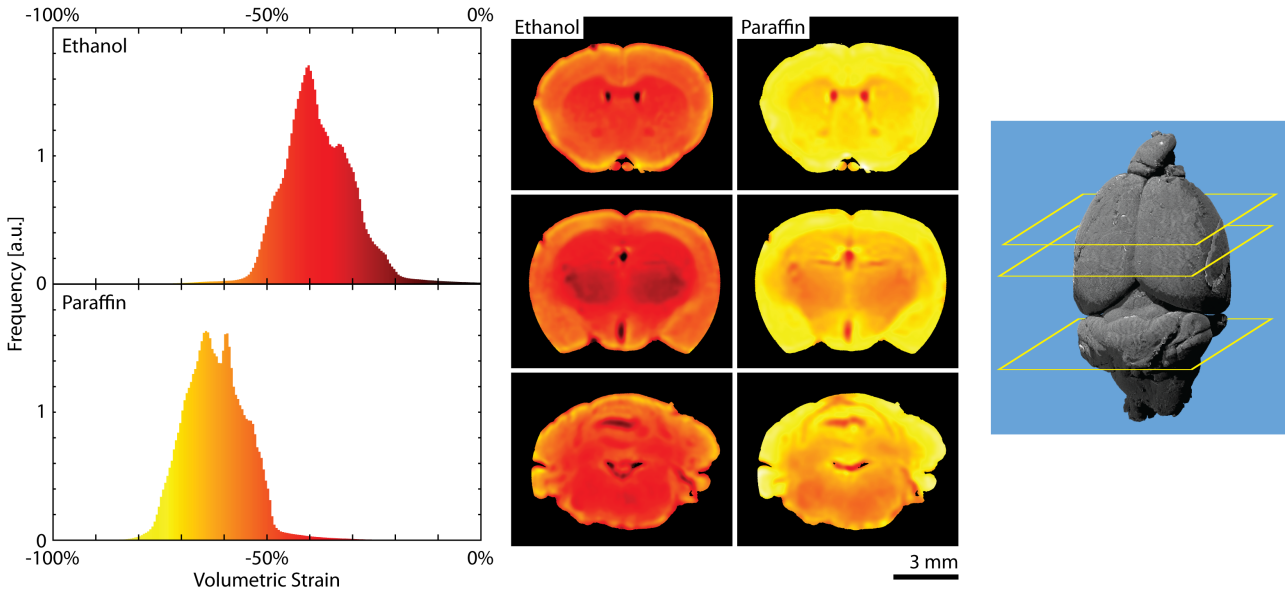

Figure 1. Volumetric strain fields represent the voxel-wise volume change from the reference space (formalin-fixed brain) to the floating space (ethanol-dehydrated or paraffin-embedded brain). Volumetric strain fields for the ethanol dehydrated and paraffin embedded mouse brain are shown *via* histograms for the entire brain (left) and three virtual coronal slices (center) at the positions indicated in the volume rendering (right). Volumetric strain of 0% indicates no volume change from the formalin-fixed state. The same colormap is used for all virtual slices and is illustrated by the shading of the histograms.

The overall reduction in volume and the anatomy-dependent shrinkage should be considered when performing virtual histology of either ethanol-dehydrated or paraffin-embedded tissue. While the ethanol-dehydrated tissue showed less volume change than paraffin, both require a correction factor when comparing distance, area, or volume measurements to those found *in vivo*, *in situ*, or from formalin-dehydrated tissue. This also applies to conventional histology of paraffin-embedded tissues. This could be achieved by registration to prior magnetic resonance imaging, prior microtomography, or an atlas. Due to the shrinkage from ethanol to paraffin, a correction factor should also be considered when comparing virtual histology of ethanol-dehydrated tissue to conventional histology of sectioned paraffin-embedded tissue. The deformations induced from the sectioning procedure may warrant an additional non-rigid registration, which may include cases where microtomography is performed on paraffin embedded tissue.[6,39]

3.2 Contrast changes within the brain after registration of the 3.1 µm-voxel datasets

The registered datasets can be used to compare corresponding features across embedding protocols. We observed significant contrast changes throughout the brain, see refs. 23, 24. Here, we will highlight the changes observed in the cerebellum (Fig. 3) and the fiber tracts (Fig. 4). For context, the locations of these highlighted regions within the mouse brain are indicated in Figure 2, which is based on the Allen Mouse Brain Atlas.[40]

Figure 3 (top) shows a sagittal view of the cerebellum for the formalin-fixed and registered ethanol-dehydrated and paraffin-embedded datasets with 3.1 µm pixel size. Histograms of the absorption coefficient within the embedding medium (black), granular layer (red), molecular layer (green), and the white matter (blue) are based on manual segmentations (inset). An increased contrast between embedding material and brain tissue was observed. The granular-molecular layer contrast increased from formalin to ethanol to paraffin. The white matter had negative contrast to the molecular layer (representative of the average throughout the brain) for formalin, positive contrast for ethanol, and nearly equal for paraffin. Generally, the difference in mean absorption between the segmented regions increased from formalin to ethanol to paraffin. The three measurements were taken with the same acquisition settings, therefore increased width of the absorption coefficient distributions in ethanol and

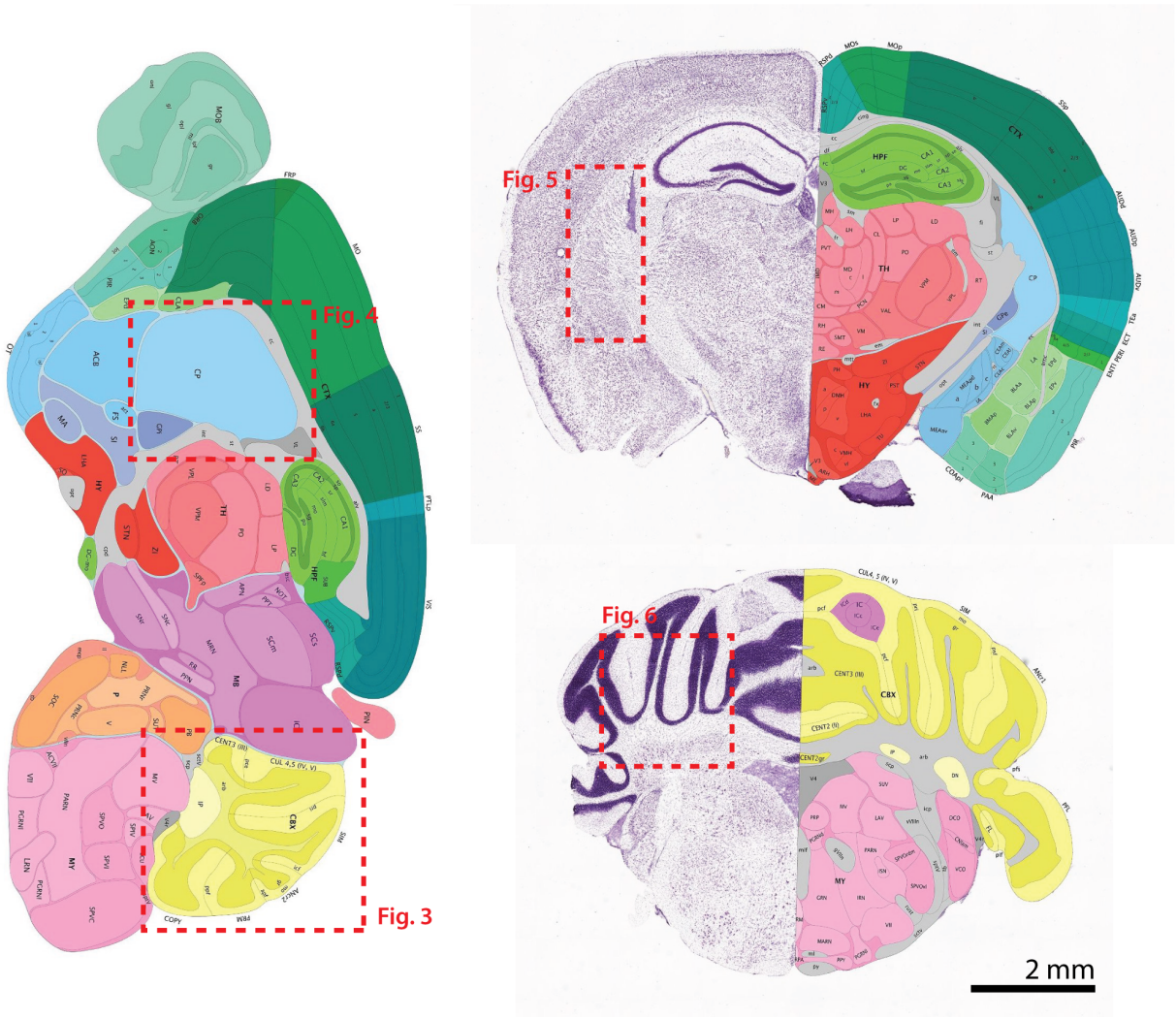

Figure 2. Regions of interest for comparison of contrast. (left) Regions of interest for the comparison of the microtomography with 3.1 µm-voxels in Figures 3 and 4 are shown within a sagittal slice from the Allen Mouse Brain Reference Atlas.[40] (right) Regions of interest for comparison of the microtomography with 0.65 µm-voxels in Figures 5 and 6 are indicated in two coronal sections.

paraffin corresponds to increased contrast of detailed structures within the segmented anatomical regions. This suggests that those two preparations are better-suited for higher resolution studies.

The most dramatic contrast changes were observed within the fiber tracts throughout the brain. Figure 4 (left) shows virtual sagittal slices in the caudoputamen for the formalin-fixed, registered ethanol-dehydrated, and registered paraffin-embedded brain. The contrast of the fibers is enhanced by ethanol-dehydration, allowing for simplified segmentation of the fiber tracts (right, volume rendering). The contrast of the fiber tracts is much reduced for the paraffin-embedded brain. We hypothesize that the myelin water is the source of the observed contrast changes.[24]

3.3 Comparison of contrast within the phase-retrieved 0.65 µm-voxel datasets

The contrast changes observed in the cerebellum (Fig. 3) and fiber tracts of the caudoputamen (Fig. 4) were further examined with follow-up imaging at a pixel size of 0.65 µm. Figure 2 (right) shows the regions examined within coronal sections from the Allen Mouse Brain Reference Atlas.[40] Two separate brains were used in

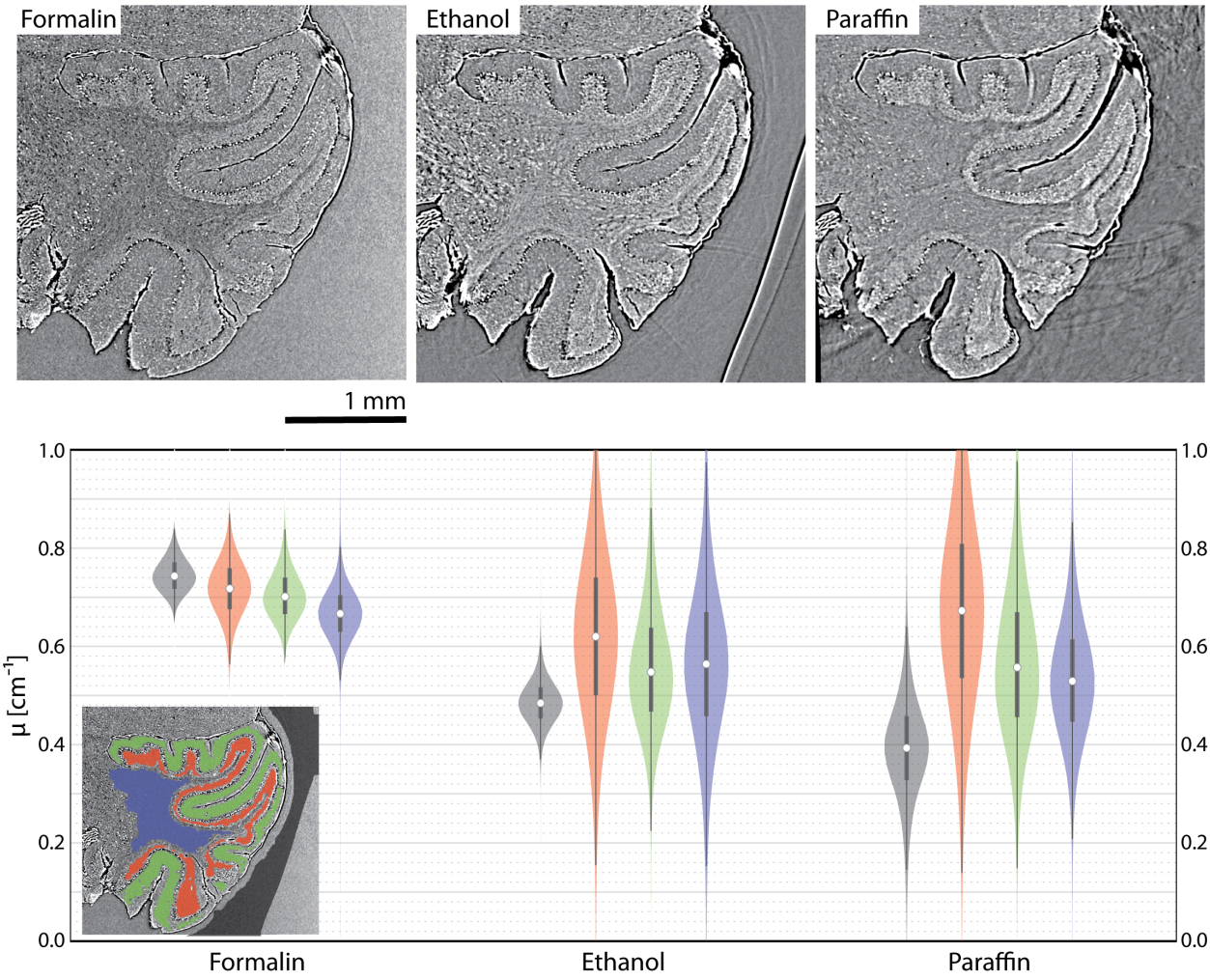

Figure 3. Comparison of X-ray contrast in the cerebellum. Virtual sagittal slices through the registered 3.1 µm-voxel datasets are given for the formalin, ethanol, and paraffin states (top). The grayscale range is given by the mean ±2.5 standard deviations of the pixel intensities throughout the entire brain. The distributions of absorption coefficient μ within the embedding medium (black), granular layer (red), molecular layer (green) and white matter (blue) are plotted (bottom). The segmentations used are shown in the inset.

this experiment, one dehydrated in ethanol and another embedded in paraffin, therefore no registration was performed. Approximately corresponding coronal slices were found by comparison with the atlas.

Figure 5 compares the ethanol-dehydrated (top) and paraffin-embedded brains (bottom) for the visualization of the fiber tracts within the caudate putamen. Here, the ethanol-dehydrated brain provides positive contrast and paraffin-embedded brain provided negative contrast for fiber tracts, illustrated best in the $\delta/\beta = 500$ reconstructions (yellow arrows). Surprisingly, despite the increase in contrast of the entire fiber tracts in ethanol, visualization of sub-structure orientation appeared easier for the paraffin embedded brain (within fiber tract indicated by the yellow arrow). Both tissue preparations allow for reasonable visualization of cells and vessels. Increasing δ/β led to only minor loss of spatial resolution, though ring- and low-frequency artefacts became stronger. Qualitatively, it appeared that $\delta/\beta = 200$ or 500 provided the best image quality.

Figure 6 compares ethanol-dehydration (left) and paraffin-embedding (right) for the visualization of the cerebellum. The 0.65 µm-voxel datasets revealed the same trends as the 3.1 µm-voxel datasets (see Fig. 3), namely the low (high) contrast between granular layer and white matter for ethanol-dehydrated (paraffin-embedded)

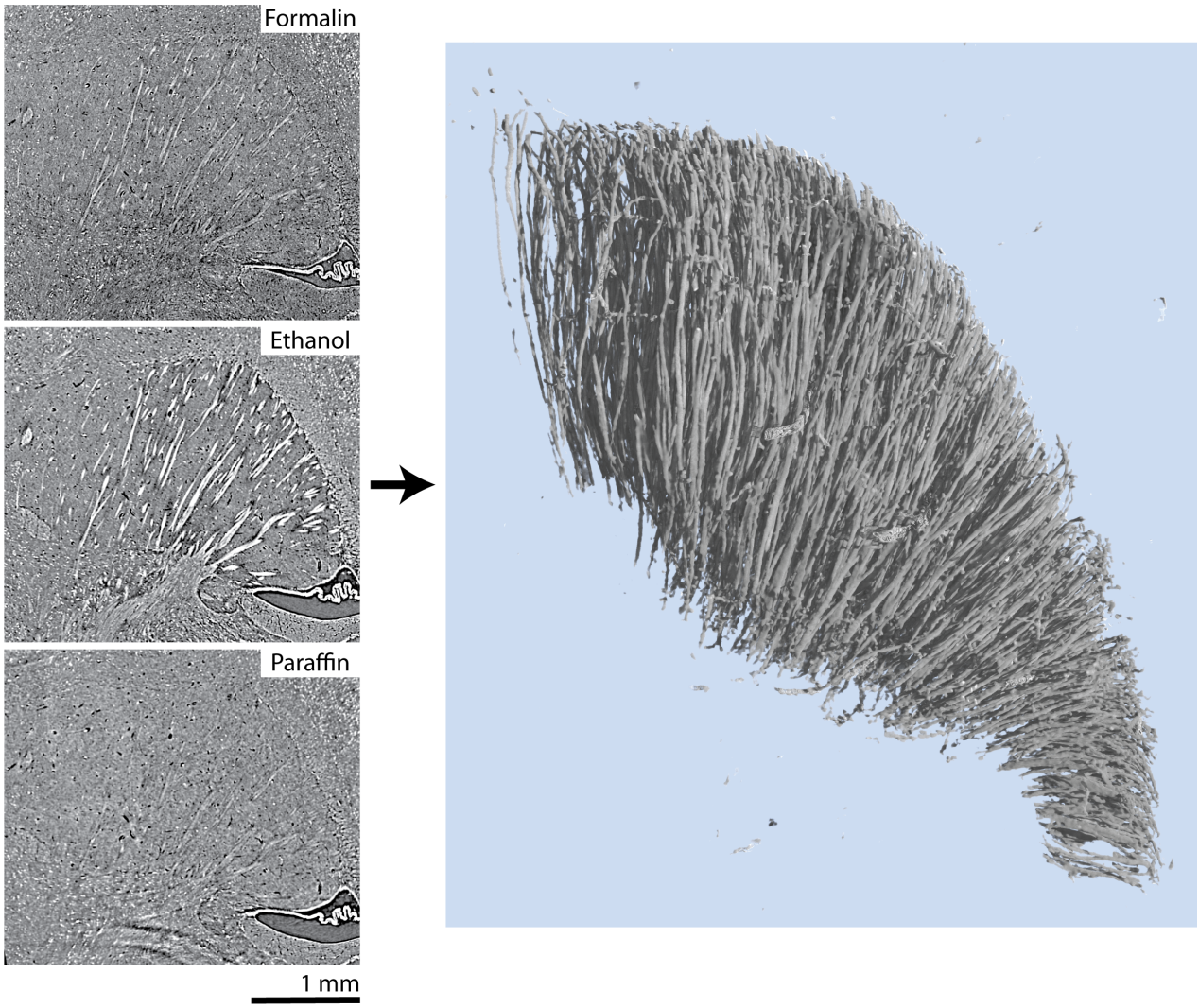

Figure 4. Enhancement of X-ray contrast in the fiber tracts as seen in the 3.1 µm-voxel datasets. Regions of interest from virtual sagittal slices through the registered datasets from formalin, ethanol, and paraffin show the caudoputamen and fiber tracts (left). Fiber tract contrast was highest in ethanol, facilitating semi-automatic segmentation (right, volume rendering of segmentation). The grayscale range is given by the mean ±2.5 standard deviations of the pixel intensities throughout the entire brain.

tissue. Both tissue preparations showed high contrast between granular and molecular layers. Higher resolution imaging revealed that paraffin-embedding led to a more uniform appearance of the molecular layer between cells. A δ/β ratio of 48 achieved a reasonable visualization of the cerebellum for the paraffin-embedded brain (cf. Fig. 5, where $\delta/\beta = 200$ or 500 were preferable).

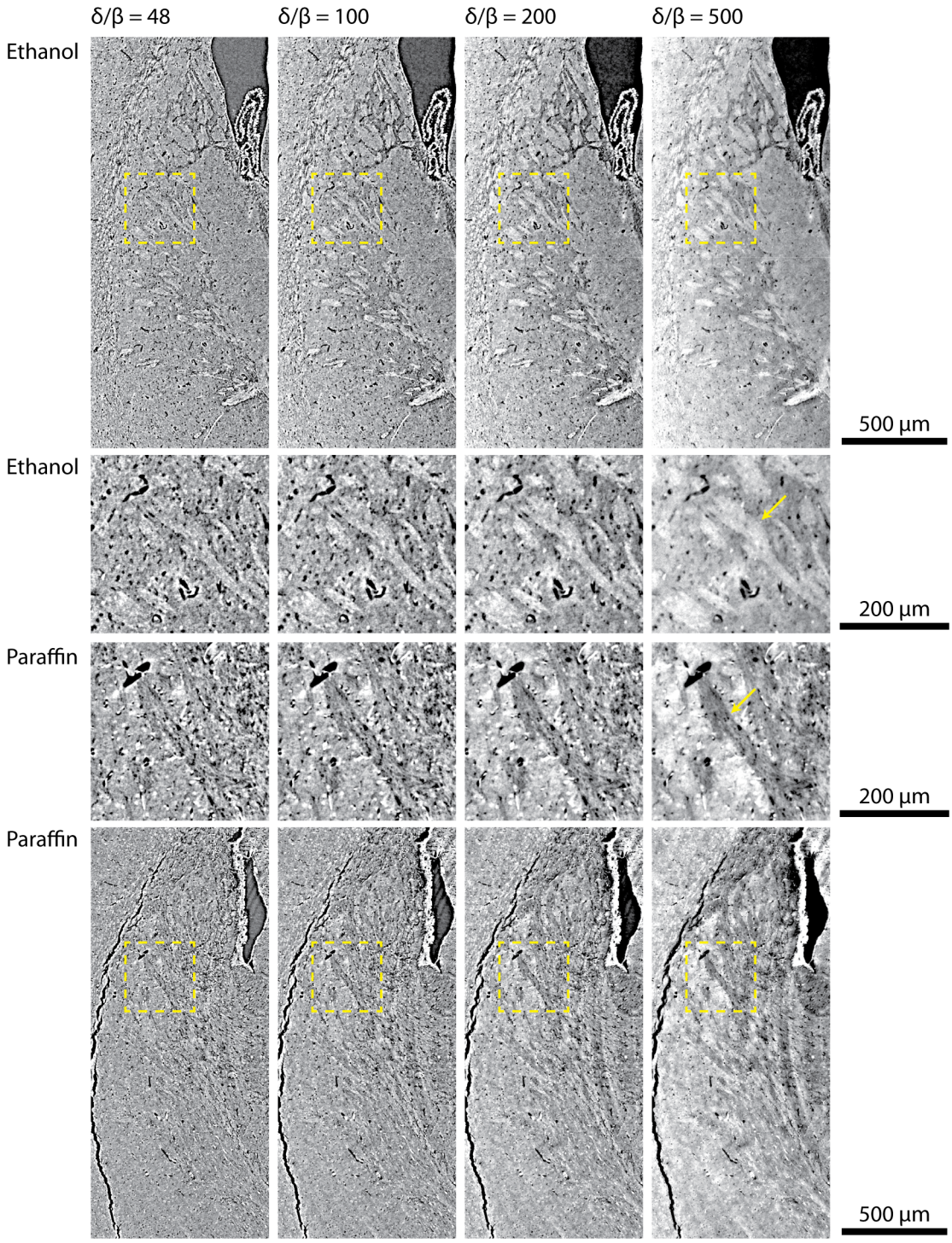

Figure 5. Comparing ethanol dehydration and paraffin embedding for the visualization of the caudate putamen and fiber tracts based on X-ray microtomography with 0.65 µm-wide voxels. Similar regions-of-interest within the ethanol-dehydrated (top) and paraffin-embedded (bottom) mouse brains are shown. Arrows in the magnified views indicate fiber tracts. Phase retrieval with Paganin's filter was applied with ascending δ/β values (left to right). Note that two separate brains were used and no registration was performed. Grayscale ranges are given by the 5th to 95th percentile of intensities present in the larger region-of-interest.

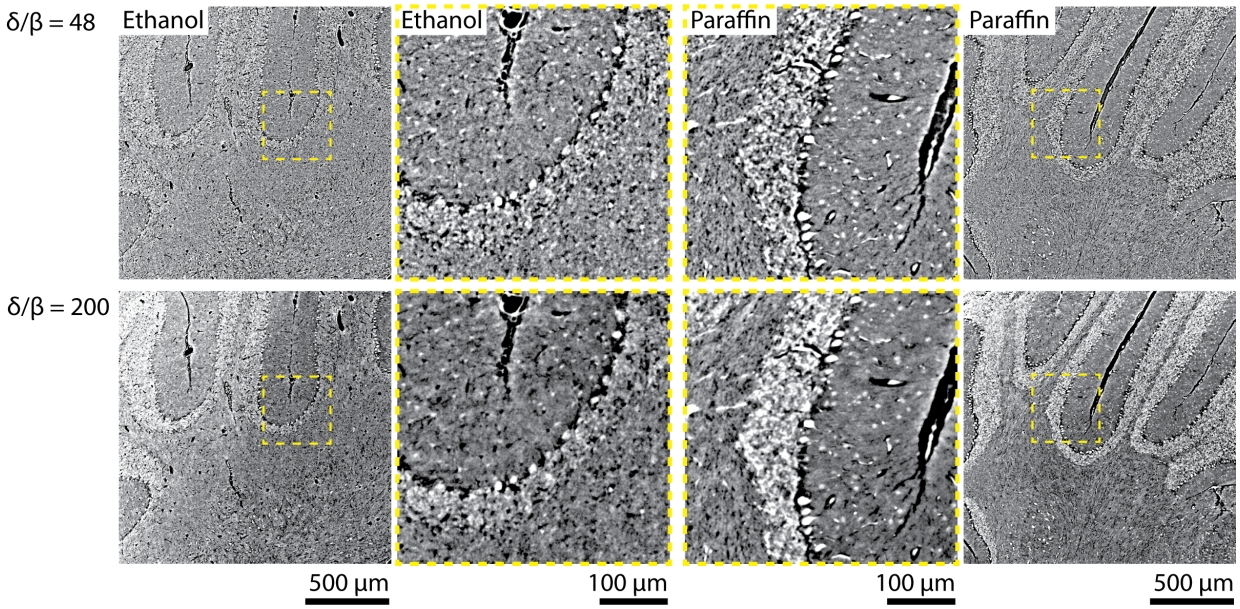

Figure 6. Regions-of-interest in the cerebellum of the ethanol-dehydrated (columns 1 and 2) and paraffin-embedded brains (columns 3 and 4) are displayed from the reconstructions with 0.65 µm-wide voxels after phase retrieval with $\delta/\beta = 48$ and 200. Magnified views (yellow dashed boxes, columns 2 and 3) display the molecular layer, granular layer, and white matter. Grayscale ranges are given by the 5th to 95th percentile of intensities present in the larger region-of-interest.

4. CONCLUSION

Non-rigid registration of 3.1 µm-voxel microtomography datasets of an entire mouse brain at the intermediate steps of formalin fixation and paraffin embedding allowed for the characterization of preparation-induced morphological and X-ray contrast changes (see also refs. 22–24). Ethanol dehydration and paraffin embedding are preferable for virtual histology thanks to improved contrast, though both lead to significant inhomogenous volume changes relative to the formalin-fixed state. Ethanol dehydration enhances white matter contrast and provides benefits for the segmentation of fiber tracts. The paraffin-embedded brain provided better contrast between the layers of the cerebellum. Follow-up imaging with 0.65 µm-voxels showed similar contrast changes. Further experiments are needed to uncover the effect of the preparations on the tissue nanostructure. With appropriate phase retrieval, both ethanol dehydration and paraffin embedding are well-suited for label-free visualization of the entire mouse brain's microanatomy. This virtual histology should be combined with MRI and conventional histology as part of a multi-modal approach for future brain atlases.

ACKNOWLEDGMENTS

Beamtime at ANATOMIX beamline, Synchrotron SOLEIL was granted under proposals 20190424 and 20200712. ANATOMIX is an Equipment of Excellence (EQUIPEX) funded by the Investments for the Future program of the French National Research Agency (ANR), project NanoimagesX, grant no. ANR-11-EQPX-0031. The authors thank J. Perrin and D. Guillaume of the ANATOMIX beamline at Synchrotron SOLEIL for support during the beam time. W.K. and V.K. acknowledge support from the Swiss National Science Foundation *via* NCCR Kidney.ch. V.K. acknowledges support from the Swiss National Science Foundation project no. 182683. G.R., C.T., M.O., and B.M. acknowledge support from the Swiss National Science Foundation project no. 185058.

REFERENCES

[1] Lichtman, J. W. and Denk, W., "The Big and the Small: Challenges of Imaging the Brain's Circuits," *Science* **334**(6056), 618–623 (2011).

[2] Tsai, P. S., Friedman, B., Ifarraguerri, A. I., Thompson, B. D., Lev-Ram, V., Schaffer, C. B., Xiong, Q., Tsien, R. Y., Squier, J. A., and Kleinfeld, D., "All-Optical Histology Using Ultrashort Laser Pulses," *Neuron* **39**(1), 27–41 (2003).

[3] Dodt, H.-U., Leischner, U., Schierloh, A., Jährling, N., Mauch, C. P., Deininger, K., Deussing, J. M., Eder, M., Zieglgänsberger, W., and Becker, K., "Ultramicroscopy: Three-dimensional visualization of neuronal networks in the whole mouse brain," *Nature Methods* **4**(4), 331–336 (2007).

[4] Denk, W. and Horstmann, H., "Serial Block-Face Scanning Electron Microscopy to Reconstruct Three-Dimensional Tissue Nanostructure," *PLOS Biology* **2**(11), e329 (2004).

[5] Albers, J., Pacilé, S., Markus, M. A., Wiart, M., Vande Velde, G., Tromba, G., and Dullin, C., "X-ray-Based 3D Virtual Histology—Adding the Next Dimension to Histological Analysis," *Molecular Imaging and Biology* **20**(5), 732–741 (2018).

[6] Khimchenko, A., Deyhle, H., Schulz, G., Schweighauser, G., Hench, J., Chicherova, N., Bikis, C., Hieber, S. E., and Müller, B., "Extending two-dimensional histology into the third dimension through conventional micro computed tomography," *NeuroImage* **139**, 26–36 (2016).

[7] Khimchenko, A., Bikis, C., Pacureanu, A., Hieber, S. E., Thalmann, P., Deyhle, H., Schweighauser, G., Hench, J., Frank, S., Müller-Gerbl, M., Schulz, G., Cloetens, P., and Müller, B., "Hard X-Ray Nanoholotomography: Large-Scale, Label-Free, 3D Neuroimaging beyond Optical Limit," *Advanced Science* **5**(6), 1700694 (2018).

[8] Kuan, A. T., Phelps, J. S., Thomas, L. A., Nguyen, T. M., Han, J., Chen, C.-L., Azevedo, A. W., Tuthill, J. C., Funke, J., Cloetens, P., Pacureanu, A., and Lee, W.-C. A., "Dense neuronal reconstruction through X-ray holographic nano-tomography," *Nature Neuroscience* **23**(12), 1637–1643 (2020).

[9] Du, M., Di, Z., Gürsoy, D., Xian, R. P., Kozorovitskiy, Y., and Jacobsen, C., "Upscaling X-ray nanoimaging to macroscopic specimens," *Journal of Applied Crystallography* **54**(2), 386–401 (2021).

[10] Hieber, S. E., Bikis, C., Khimchenko, A., Schweighauser, G., Hench, J., Chicherova, N., Schulz, G., and Müller, B., "Tomographic brain imaging with nucleolar detail and automatic cell counting," *Scientific Reports* **6**(1), 32156 (2016).

[11] Dyer, E. L., Roncal, W. G., Prasad, J. A., Fernandes, H. L., Gürsoy, D., Andrade, V. D., Fezzaa, K., Xiao, X., Vogelstein, J. T., Jacobsen, C., Körding, K. P., and Kasthuri, N., "Quantifying Mesoscale Neuroanatomy Using X-Ray Microtomography," *eNeuro* **4**(5) (2017).

[12] Töpperwien, M., van der Meer, F., Stadelmann, C., and Salditt, T., "Three-dimensional virtual histology of human cerebellum by X-ray phase-contrast tomography," *Proceedings of the National Academy of Sciences* **115**(27), 6940–6945 (2018).

[13] Massimi, L., Bukreeva, I., Santamaria, G., Fratini, M., Corbelli, A., Brun, F., Fumagalli, S., Maugeri, L., Pacureanu, A., Cloetens, P., Pieroni, N., Fiordaliso, F., Forloni, G., Uccelli, A., Kerlero de Rosbo, N., Balducci, C., and Cedola, A., "Exploring Alzheimer's disease mouse brain through X-ray phase contrast tomography: From the cell to the organ," *NeuroImage* **184**, 490–495 (2019).

[14] Prasad, J. A., Balwani, A. H., Johnson, E. C., Miano, J. D., Sampathkumar, V., De Andrade, V., Fezzaa, K., Du, M., Vescovi, R., Jacobsen, C., Kording, K. P., Gürsoy, D., Gray Roncal, W., Kasthuri, N., and Dyer, E. L., "A three-dimensional thalamocortical dataset for characterizing brain heterogeneity," *Scientific Data* **7**(1), 358 (2020).

[15] Vescovi, R., Du, M., de Andrade, V., Scullin, W., Gürsoy, D., and Jacobsen, C., "Tomosaic: Efficient acquisition and reconstruction of teravoxel tomography data using limited-size synchrotron X-ray beams," *Journal of Synchrotron Radiation* **25**(5), 1478–1489 (2018).

[16] Miettinen, A., Oikonomidis, I. V., Bonnin, A., and Stampanoni, M., "NRStitcher: Non-rigid stitching of terapixel-scale volumetric images," *Bioinformatics* **35**(24), 5290–5297 (2019).

[17] Trinkle, S., Foxley, S., Kasthuri, N., and Rivière, P. L., "Synchrotron X-ray micro-CT as a validation dataset for diffusion MRI in whole mouse brain," *Magnetic Resonance in Medicine* **86**(2), 1067–1076 (2021).

[18] Foxley, S., Sampathkumar, V., De Andrade, V., Trinkle, S., Sorokina, A., Norwood, K., La Riviere, P., and Kasthuri, N., "Multi-modal imaging of a single mouse brain over five orders of magnitude of resolution," *NeuroImage* **238**, 118250 (2021).

[19] Mitra, P. P., "The Circuit Architecture of Whole Brains at the Mesoscopic Scale," *Neuron* **83**(6), 1273–1283 (2014).

[20] Töpperwien, M., Markus, A., Alves, F., and Salditt, T., "Contrast enhancement for visualizing neuronal cytoarchitecture by propagation-based x-ray phase-contrast tomography," *NeuroImage* **199**, 70–80 (2019).

[21] Quester, R. and Schröder, R., "The shrinkage of the human brain stem during formalin fixation and embedding in paraffin," *Journal of Neuroscience Methods* **75**(1), 81–89 (1997).

[22] Rodgers, G., Schulz, G., Kuo, W., Scheel, M., Kurtcuoglu, V., Weitkamp, T., Müller, B., and Tanner, C., "Non-rigid registration to determine strain fields during mouse brain fixation and embedding," in [*Bioinspiration, Biomimetics, and Bioreplication XI*], **11586**, 115860I, International Society for Optics and Photonics (2021).

[23] Rodgers, G., Kuo, W., Schulz, G., Scheel, M., Migga, A., Bikis, C., Tanner, C., Kurtcuoglu, V., Weitkamp, T., and Müller, B., "Virtual histology of an entire mouse brain from formalin fixation to paraffin embedding. Part 1: Data acquisition, anatomical feature segmentation, global volume and density tracking," *Journal of Neuroscience Methods* (2021). submitted.

[24] Rodgers, G., Tanner, C., Schulz, G., Migga, A., Kuo, W., Bikis, C., Scheel, M., Kurtcuoglu, V., Weitkamp, T., and Müller, B., "Virtual histology of an entire mouse brain from formalin fixation to paraffin embedding. Part 2: Volumetric strain fields and local contrast changes," *Journal of Neuroscience Methods* (2021). submitted.

[25] Wolfe, D., "6 - Tissue processing," in [*Bancroft's Theory and Practice of Histological Techniques (Eighth Edition)*], Suvarna, S. K., Layton, C., and Bancroft, J. D., eds., 73–83, Elsevier (2019).

[26] Weitkamp, T., Scheel, M., Giorgetta, J. L., Joyet, V., Roux, V. L., Cauchon, G., Moreno, T., Polack, F., Thompson, A., and Samama, J. P., "The tomography beamlineANATOMIXat Synchrotron SOLEIL," *Journal of Physics: Conference Series* **849**, 012037 (2017).

[27] Desjardins, K., Carcy, A., Giorgetta, J.-L., Menneglier, C., Scheel, M., and Weitkamp, T., "Design of Indirect X-Ray Detectors for Tomography on the Anatomix Beamline," in [*Mechanical Eng.˜Design of Synchrotron Radiation Equipment and Instrumentation (MEDSI'18), Paris, France, 25-29 June 2018*], 355–357, JACOW Publishing, Geneva, Switzerland (2018).

[28] Weitkamp, T., Haas, D., Wegrzynek, D., and Rack, A., "ANKAphase: Software for single-distance phase retrieval from inline X-ray phase-contrast radiographs," *Journal of Synchrotron Radiation* **18**(4), 617–629 (2011).

[29] Kyrieleis, A., Ibison, M., Titarenko, V., and Withers, P. J., "Image stitching strategies for tomographic imaging of large objects at high resolution at synchrotron sources," *Nuclear Instruments and Methods in Physics Research Section A: Accelerators, Spectrometers, Detectors and Associated Equipment* **607**(3), 677–684 (2009).

[30] Vo, N. T., Atwood, R. C., Drakopoulos, M., and Connolley, T., "Data processing methods and data acquisition for samples larger than the field of view in parallel-beam tomography," *Optics Express* **29**(12), 17849–17874 (2021).

[31] Boin, M. and Haibel, A., "Compensation of ring artefacts in synchrotron tomographic images," *Optics Express* **14**(25), 12071–12075 (2006).

[32] Mirone, A., Brun, E., Gouillart, E., Tafforeau, P., and Kieffer, J., "The PyHST2 hybrid distributed code for high speed tomographic reconstruction with iterative reconstruction and a priori knowledge capabilities," *Nuclear Instruments and Methods in Physics Research Section B: Beam Interactions with Materials and Atoms* **324**, 41–48 (2014).

[33] Rodgers, G., Schulz, G., Deyhle, H., Kuo, W., Rau, C., Weitkamp, T., and Müller, B., "Optimizing contrast and spatial resolution in hard x-ray tomography of medically relevant tissues," *Applied Physics Letters* **116**(2), 023702 (2020).

[34] Klein, S., Staring, M., Murphy, K., Viergever, M. A., and Pluim, J. P. W., "Elastix: A Toolbox for Intensity-Based Medical Image Registration," *IEEE Transactions on Medical Imaging* **29**(1), 196–205 (2010).

[35] Shamonin, D. P., Bron, E. E., Lelieveldt, B. P. F., Smits, M., Klein, S., and Staring, M., "Fast Parallel Image Registration on CPU and GPU for Diagnostic Classification of Alzheimer's Disease," *Frontiers in Neuroinformatics* **0** (2014).

[36] Paganin, D., Mayo, S. C., Gureyev, T. E., Miller, P. R., and Wilkins, S. W., "Simultaneous phase and amplitude extraction from a single defocused image of a homogeneous object," *Journal of Microscopy* **206**(1), 33–40 (2002).

[37] Gürsoy, D., De Carlo, F., Xiao, X., and Jacobsen, C., "TomoPy: A framework for the analysis of synchrotron tomographic data," *Journal of Synchrotron Radiation* **21**(5), 1188–1193 (2014).

[38] Marone, F. and Stampanoni, M., "Regridding reconstruction algorithm for real-time tomographic imaging," *Journal of Synchrotron Radiation* **19**(6), 1029–1037 (2012).

[39] Germann, M., Morel, A., Beckmann, F., Andronache, A., Jeanmonod, D., and Müller, B., "Strain fields in histological slices of brain tissue determined by synchrotron radiation-based micro computed tomography," *Journal of Neuroscience Methods* **170**(1), 149–155 (2008).

[40] Lein, E. S., Hawrylycz, M. J., Ao, N., Ayres, M., Bensinger, A., Bernard, A., Boe, A. F., Boguski, M. S., Brockway, K. S., Byrnes, E. J., Chen, L., Chen, L., Chen, T.-M., Chi Chin, M., Chong, J., Crook, B. E., Czaplinska, A., Dang, C. N., Datta, S., Dee, N. R., Desaki, A. L., Desta, T., Diep, E., Dolbeare, T. A., Donelan, M. J., Dong, H.-W., Dougherty, J. G., Duncan, B. J., Ebbert, A. J., Eichele, G., Estin, L. K., Faber, C., Facer, B. A., Fields, R., Fischer, S. R., Fliss, T. P., Frensley, C., Gates, S. N., Glattfelder, K. J., Halverson, K. R., Hart, M. R., Hohmann, J. G., Howell, M. P., Jeung, D. P., Johnson, R. A., Karr, P. T., Kawal, R., Kidney, J. M., Knapik, R. H., Kuan, C. L., Lake, J. H., Laramee, A. R., Larsen, K. D., Lau, C., Lemon, T. A., Liang, A. J., Liu, Y., Luong, L. T., Michaels, J., Morgan, J. J., Morgan, R. J., Mortrud, M. T., Mosqueda, N. F., Ng, L. L., Ng, R., Orta, G. J., Overly, C. C., Pak, T. H., Parry, S. E., Pathak, S. D., Pearson, O. C., Puchalski, R. B., Riley, Z. L., Rockett, H. R., Rowland, S. A., Royall, J. J., Ruiz, M. J., Sarno, N. R., Schaffnit, K., Shapovalova, N. V., Sivisay, T., Slaughterbeck, C. R., Smith, S. C., Smith, K. A., Smith, B. I., Sodt, A. J., Stewart, N. N., Stumpf, K.-R., Sunkin, S. M., Sutram, M., Tam, A., Teemer, C. D., Thaller, C., Thompson, C. L., Varnam, L. R., Visel, A., Whitlock, R. M., Wohnoutka, P. E., Wolkey, C. K., Wong, V. Y., Wood, M., Yaylaoglu, M. B., Young, R. C., Youngstrom, B. L., Feng Yuan, X., Zhang, B., Zwingman, T. A., and Jones, A. R., "Genome-wide atlas of gene expression in the adult mouse brain," *Nature* **445**(7124), 168–176 (2007).